ACS OMEGA

Article

Cite This: ACS Omega 2019, 4, 1434−1442

http://pubs.acs.org/journal/acsodf

First-Principles Evaluation of the Morphology of WS_2 Nanotubes for Application as Visible-Light-Driven Water-Splitting Photocatalysts

Sergei Piskunov,*[,†] Oleg Lisovski,[†] Yuri F. Zhukovskii,[†] Pavel N. D'yachkov,[‡] Robert A. Evarestov,[§] Stephane Kenmoe,[∥] and Eckhard Spohr[∥]

[†]Institute of Solid State Physics, University of Latvia, Kengaraga 8, LV-1063 Riga, Latvia

[‡]Institute of General and Inorganic Chemistry, Russian Academy of Science, Leninskii prosp. 31, 119991 Moscow, Russia

[§]Institute of Chemistry, Saint Petersburg State University, Universitetskaya nab. 7/9, 199034 Saint Petersburg, Russia

[∥]Theoretical Chemistry Department, University of Duisburg-Essen, Universitätstr. 2, 45141 Essen, Germany

ABSTRACT: One-dimensional tungsten disulfide (WS_2) single-walled nanotubes (NTs) with either achiral, i.e., armchair (n, n) and zigzag-type (n, 0), or chiral ($2n$, n) configuration with diameters d_{NT} > 1.9 nm have been found to be suitable for photocatalytic applications, since their band gaps correspond to the frequency range of visible light between red and violet (1.5 eV < $\Delta\varepsilon_{gap}$ < 2.6 eV). We have simulated the electronic structure of nanotubes with diameters up to 12.0 nm. The calculated top of the valence band and the bottom of the conduction band (ε_{VB} and ε_{CB}, respectively) have been properly aligned relatively to the oxidation (ε_{O_2/H_2O}) and reduction (ε_{H_2/H_2O}) potentials of water. Very narrow nanotubes (0.5 < d_{NT} < 1.9 nm) are unsuitable for water splitting because the condition $\varepsilon_{VB} < \varepsilon_{O_2/H_2O} < \varepsilon_{H_2/H_2O} < \varepsilon_{CB}$ does not hold. For nanotubes with d_{NT} > 1.9 nm, the condition $\varepsilon_{VB} < \varepsilon_{O_2/H_2O} < \varepsilon_{H_2/H_2O} < \varepsilon_{CB}$ is fulfilled. The values of ε_{VB} and ε_{CB} have been found to depend only on the diameter and not on the chirality index of the nanotube. The reported structural and electronic properties have been obtained from either hybrid density functional theory and Hartree−Fock linear combination of atomic orbitals calculations (using the HSE06 functional) or the linear augmented cylindrical waves density functional theory method. In addition to single-walled NTs, we have investigated a number of achiral double-walled (m, m)@(n, n) and (m, 0)@(n, 0) as well as triple-walled (l, l)@(m, m)@(n, n) and (l, 0)@(m, 0)@(n, 0) nanotubes. All multiwalled nanotubes show a common dependence of their band gap on the diameter of the inner nanotube, independent of chirality index and number of walls. This behavior of WS_2 NTs allows the exploitation of the entire range of the visible spectrum by suitably tuning the band gap.

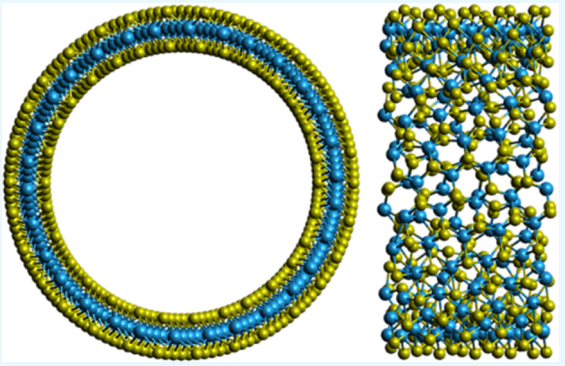

I. INTRODUCTION

Despite substantial progress in science and technology of renewable energy strategies in the last decades, many fundamental issues still need to be addressed. One of the possibilities to substitute fossil fuel consumption by an alternative based on renewable sources is to develop efficient catalysts for solar hydrogen generation from water. Such catalysts have been known already for about 40 years, beginning with the pioneering work of Honda and Fujishima.[1] However, such catalysts are not yet economically competitive for hydrogen production, since competitiveness would require conversion efficiencies higher than the currently achieved values of slightly more than 10%.[2]

Anatase- and rutile-structured TiO_2 were used in the pioneering work and have been extensively studied to date. TiO_2 gained attention due to its range of favorable properties[3] such as chemical stability, photocorrosion resistance, water insolubility, nontoxicity, low cost, and natural abundance. However, while the position of the conduction band bottom is quite beneficial, the top of the valence band of titania is far from the desired level, and the band gap is too wide (3.2 eV for bulk anatase vs 3.0 eV for rutile bulk), requiring energies near the ultraviolet edge of the solar spectrum and thus outside the range of visible light. This wide band gap leads to the necessity to either manipulate the properties of TiO_2 and other binary and ternary transition-metal oxides[4] or study other prospective materials. In the first case, since most band gaps were found to be too wide (≥3.0 eV), doping the material with certain substitutional atoms could result in the appearance of additionally induced levels inside the band gap, thus creating new optical absorption edges and reducing the energy threshold necessary for adsorption of visible-light photons.[5] On the other hand, alternative nonoxide layered materials, in particular transition-metal chalcogenides, gained growing

Received: November 23, 2018
Accepted: January 8, 2019
Published: January 16, 2019

DOI: 10.1021/acsomega.8b03121
ACS Omega 2019, 4, 1434−1442

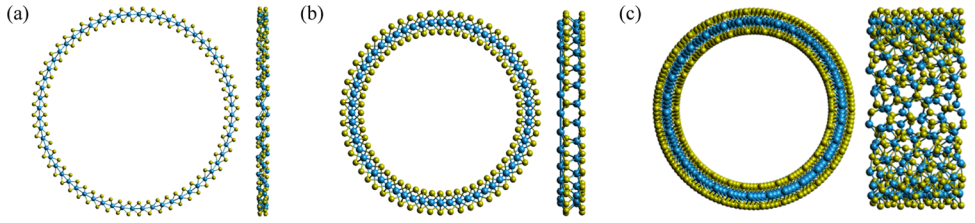

Figure 1. Three types of WS_2 SWNTs with different chiralities modeled in this study: (a) armchair (12, 12), (b) zigzag (21, 0), and (c) chiral (16, 8). The left-hand side of each subfigure corresponds to the NT cross section, while the right-hand side depicts the side view of the NT unit cell.

attention in the last years, since they possess significantly narrower band gaps than transition-metal oxides. One of them is tungsten disulfide WS_2. The band gap of bulk WS_2 was measured to be ∼1.4 eV,[6] corresponding to the near-infrared, invisible range of the light spectrum.

The hexagonal 2H c phase of bulk WS_2 possesses a graphite-like structure, consisting of layers formed by three atomic planes (S−W−S); the WS_2 layers interact only via weak interlayer van der Waals forces.[7] Although bulk WS_2 was found to suffer from photocorrosion, which essentially destroys its photocatalytic suitability,[8] a noticeable strengthening of its resistance to this undesirable process can be achieved by the transition from three-dimensional (3D) material structures to those of lower dimensionality, e.g., thin two-dimensional (2D) nanofilms.[9] The fundamental band gap for the single-monolayer (1 ML) WS_2(0001) nanosheet (when supported by Si[10] or α-Al_2O_3 substrates[11]) was experimentally found to be 2.4 eV, significantly larger than that of bulk WS_2 (1.4 eV). The band gap edges ε_{VB} and ε_{CB} of tungsten disulfide are properly aligned relatively to the redox potentials ε_{O_2/H_2O} and ε_{H_2/H_2O} (Figure 1 in ref 9). Simultaneously, both the electron mobility and the specific amount of active sites on WS_2(0001) nanosheets were found to be noticeably higher than those on the (101) anatase facet.[9] A number of experimental and theoretical studies of pristine and defective tungsten disulfide thin nanofilms have been performed so far, e.g., those described in refs 9−17. In particular, defects formed on a single WS_2 monolayer lead to the formation of induced states in the middle of the band gap, thus opening up possibilities to form n- or p-type semiconductors in the presence of S or W vacancies, respectively.[16] However, the induced localized states would prohibit water splitting in the proximity of defective WS_2(0001), which means that only pristine or almost defectless tungsten disulfide nanosheets can be suitable for photocatalytic applications.

Hence, only one-dimensional (1D) nanostructures such as nanotubes (NTs)[18−27] and nanoribbons[28] or zero-dimensional structures such as fullerene-like nanocages[22] and nanoclusters[29,30] of WS_2 can possibly be suitable for photocatalysis. WS_2 nanotubes (NTs) were first synthesized in 1992 by the group of Tenne,[18] while their theoretical characterization is still in its infancy.[26,27] The latter studies took into account approaches based on the line symmetry group formalism, using either valence force fields combined with semiempirical density functional tight binding (DFTB) theory[26] or an ab initio hybrid density functional theory (DFT) Hartree−Fock (HF) formalism using the HSE06 functional in which the Hamiltonian of density functional theory is extended by the Hartree−Fock exchange and correlation functionals.[27] Earlier ab initio calculations of WS_2-based nanotubes by Zibouche et al.[21] compared the electronic structure of the bulk, layered, and nanotubular forms for molybdenum and tungsten disulfides. In refs 21 25 26, and 27 the vibrational and electronic properties of WS_2 NTs were calculated and analyzed, but not their possible photocatalytic applications. Among the numerous experimental studies of these nanomaterials, this point was ignored too, except for a few manuscripts directly devoted to evaluation of the photocatalytic suitability of WS_2 nanotubes. For example, Zhu et al.[20] undertook a successful attempt to synthesize Nb-doped WS_2 nanotubes, which inhibits the formation of defective NTs unlike in the synthesis of pristine nanotubes. Yadgarov et al.[22] studied controlled doping of tungsten disulfide nanotubes and fullerene-shaped structures. These authors noticed in particular that the presence of Re dopants results in a drop of the electrical resistivity, leading to more efficient electron transport through the corresponding nanotubes. Tsverin et al.[23] concluded that the significant enhancement in the photoactivity of hybrid nanostructures can be attributed to the combination of metallic Co nanoparticles and semiconducting WS_2 NTs. In the case of hybrid nanostructures, efficient light absorption by nanotubes occurs and the subsequent charge separation between the hybrid semiconductor WS_2 NT and the metallic nanocluster takes place under visible-light illumination.

This short survey leads us to conclude that, although there are numerous reports on the successful evaluation of WS_2-based catalysts for solar hydrogen generation, comprehensive investigations of sophisticated monoperiodic structures like nanotubes are rather scarce; specifically, theoretical insight into the origin of their performance is missing. We aim to fill this gap by simulating a series of WS_2 NTs, with different nanotube chiralities and diameters d_{NT} up to 12 nm. This paper is structured as follows: in Section II, the models of single-walled (SWNT), double-walled (DWNT), and triple-walled (TWNT) WS_2 NTs as well as their relevant parameters (Section II.I) are described; computational details of the ab initio calculations are given for both the linear combination of atomic orbitals (LCAO) method implemented within the hybrid DFT and HF approach (Section II.II) and the linear combination of cylindrical waves method (LACW) (Section II.III). Sections III.I and III.II compare the energetics of pristine WS_2 NTs of different sizes and chiralities for single- and multiwalled (MW) nanotubes, respectively, highlighting the corresponding conditions and limitations. In Section III.III, we compare the electronic structure of some single-walled nanotubes with different chiralities obtained by two different methods, namely, the DFT-LCAO method and the DFT-LACW method. Section IV provides a short summary of the results obtained.

II. COMPUTATIONAL DETAILS

II.I. Models of WS_2 Nanotubes. Symmetry and structure of WS_2 NTs can be described by folding the corresponding

DOI: 10.1021/acsomega.8b03121
ACS Omega 2019, 4, 1434−1442

nanolayer, i.e., construction of the cylindrical nanotubes by rolling up graphene-like 2D nanosheets with hexagonal structure using the formalism of line groups.[26,27] For this purpose, the nomenclature of single-walled (m, n) carbon nanotubes can be expressed via the so-called chirality indices m and n as described earlier.[31] Within this formalism, the nanotube diameter d_{NT} is determined as the diameter of the WS_2 cylinder defined by the centers of the tungsten atoms

$$d_{NT} = \frac{L}{\pi} = a\sqrt{m^2 + mn + n^2} \quad (1)$$

where L is the circumferential length of the WS_2 SWNTs, while $a = 0.315$ nm[7] is the lattice constant of the WS_2 monolayer. To study the properties of SWNTs as a function of diameter and chirality index, in either the achiral (possessing armchair (n, n) and zigzag-type $(n, 0)$ morphologies) or the chiral $(2n, n)$ configuration, we have performed large-scale ab initio calculations of their electronic structure, in which we vary the diameter d_{NT} from about 1.0−12.0 nm by varying n (Figure 1).

For multiwalled (MW) NTs, only achiral configurations were modeled due to the high computational cost for the chiral $(2n, n)$ NTs with their extended unit cell along the nanotube axis. Cross sections of the achiral double-walled $(m, m)@(n, n)$ and $(m, 0)@(n, 0)$ nanotubes (DWNTs) as well as triple-walled $(l, l)@(m, m)@(n, n)$ and $(l, 0)@(m, 0)@(n, 0)$ nanotubes (TWNTs) are shown in Figures 2 and 3, respectively.

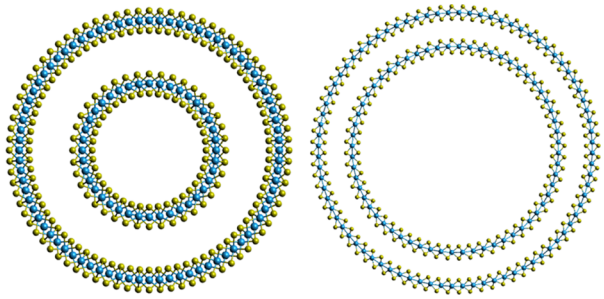

Figure 2. Cross sections of (50, 0)@(30, 0) (left) and (40, 40)@(30, 30) (right) WS_2 DWNTs.

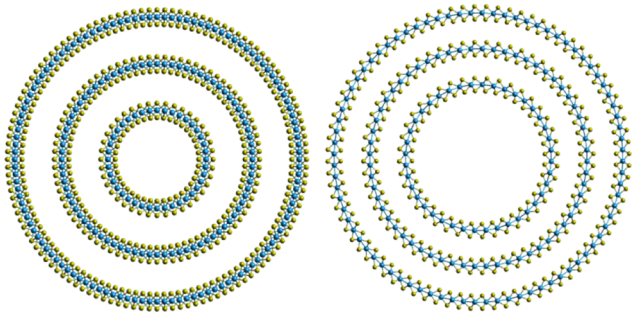

Figure 3. Cross sections of (60, 0)@(40, 0)@(20, 0) (left) and (40, 40)@(30, 30)@(20, 20) (right) WS_2 TWNTs.

II.II. Hybrid DFT and HF-LCAO Method. In the present study, we have performed hybrid density functional theory (DFT) calculations using the CRYSTAL14 computer code,[32] which utilizes localized Gaussian-type functions in the form of atom-centered basis sets (BSs) for expansion of periodic crystalline orbitals as linear combinations of atomic orbitals (LCAO). In our earlier paper,[33] we used the PBE0 hybrid functional for fully relaxed calculations of bulk WS_2 and could not adequately reproduce the experimental value of the band gap for the hexagonal morphology (2.51 eV (calculated) vs 1.3−1.4 eV (experimental)). On the other hand, the HSE06 hybrid functional[34,35] used in the current study proved to be much more adequate for reproducing the experimental value with the computed one of 1.58 eV. The ECP-1111s-1111p-11d[36] basis set (BS) was adopted for sulfur atoms, while for tungsten atoms, the ECP-11sp-31d56 BS was employed,[37] using an effective core pseudopotential (ECP) to accelerate the computation. To provide a balanced summation in both direct and reciprocal lattices, the reciprocal space integration was performed by sampling the Brillouin zone (BZ) with the 18 × 1 × 1 Monkhorst−Pack mesh,[38] which results in a total of 10 k-points evenly distributed over the BZ. Calculations were considered as converged only when the total energy differs by less than 10^{-9} au in two successive cycles of the self-consistent field procedure.[32]

To take into account weak interactions between adjacent walls of the MW WS_2 NTs, one can apply the Grimme dispersion correction (DC).[39] However, no noticeable influence of the DC was found on the positions of energy levels in recent ab initio simulations of multilayered $WS_2(0001)$ nanothin films.[40] On the other hand, real contribution to the interwall interactions in transition-metal disulfide nanostructures can be caused by weak repulsion between the negatively charged external S-shells.[41] Their quantitative estimate can be performed by calculating the difference between the energy of a multilayer system and the sum of energies of its constituents. Such an analysis has been performed here for MW WS_2 NTs: to this end, we have calculated the interwall interaction energies for DWNTs and TWNTs

$$E_{int}^{DWNT} = (E\{(n_1, n_1')@(n_2, n_2')\} - E\{(n_1, n_1')\} - E\{(n_2, n_2')\})/Z(DWNT) \quad (2a)$$

$$E_{int}^{TWNT} = (E\{(n_1, n_1')@(n_2, n_2')@(n_3, n_3')\} - E\{(n_1, n_1')\} - E\{(n_2, n_2')-E\{(n_3, n_3')\})/Z(TWNT) \quad (2b)$$

where $E\{(n_1, n_1')@(n_2, n_2')\} - E\{(n_1, n_1')\} - E\{(n_2, n_2')\}$ and $E\{(n_1, n_1')@(n_2, n_2')@(n_3, n_3')\} - E\{(n_1, n_1')\} - E\{(n_2, n_2')\} - E\{(n_3, n_3')\}$ stand for DW and TW nanotubes and their constituents, respectively, while Z(D(T)WNT) is the number of formula units per unit cell of the corresponding DW or TW nanotubes. Results of these quantitative estimates are presented and analyzed in Section III.I.

II.III. DFT-LACW Method. The linearized augmented cylindrical wave (LACW) technique is an extension of the linearized augmented plane-wave (LAPW) method to the specific case of one-dimensional cylindrical or tubular polyatomic systems such as the WS_2 nanotubes studied here (Figure 1). The main foundations and applications of the LACW method have been described in detail elsewhere[42−46] and are compiled in a recent review.[47] Similar to the simple version of the original LAPW theory for bulk materials, the LACW method is based on the muffin-tin (MT) and the local density exchange approximation for the electronic potential. That is, the potential $V(r)$ is constructed to be spherically symmetric $V_\alpha(r)$ in the regions of atomic cores (within the MT spheres α) and constant with a value V_0 in the region between

DOI: 10.1021/acsomega.8b03121
ACS Omega 2019, 4, 1434−1442

the atomic cores. However, a large difference exists between the bulk phase and nanomaterials because in the former case, the electron redistribution is unlimited in all spatial directions, while it is strongly confined to a thin tubular layer in NTs in the latter case. Therefore, the MT method has to be somewhat adapted to the case of tubular structures. Specifically, in the LACW method, the tubule is considered to be positioned between two impenetrable barriers Ω_a and Ω_b of cylindrical symmetry, separating the polyatomic system from the vacuum regions outside and inside the NT. The width d of the cylindrical layer between Ω_a and Ω_b becomes a parameter of the model. As a result, the electronic structure of the NTs is determined by free electron movement in the interspherical region, electron scattering by the MT spheres, and electron reflection from the cylindrical barriers Ω_a and Ω_b. Similar to the LAPW model, we also apply Slater's $\rho(r)^{1/3}$ potential for the exchange−correlation term, where the electron density ρ of the nanotube is calculated as a superposition of atomic electron densities $\rho_\alpha(r)$.

Originally, the DFT-LACW code can only perform calculations for the perfect WS_2 SWNT structures only by rolling up a WS_2 sheet without further geometry optimization of the tubules. Thereby, a symmetrized version of the LACW technique can be applied, where the unit cell of any nanotube is reduced to one formula unit, and the band structure takes a simple form. The thickness of the cylindrical layers and the reference energy have been chosen so as to reproduce the DFT-LCAO width of the band gap (1.86 eV) and the valence band top (−6.28 eV) of the (12, 12) WS_2 nanotube. Moreover, to improve agreement with the DFT-LCAO results, we have performed LACW calculations on CRYSTAL-optimized structures of WS_2 SWNTs. Some quantitative differences between the corresponding densities of states (DOSs) for the initial (Figure 1) and CRYSTAL-optimized configurations of nanotubes are visible (see below). For example, the ratios of intensities between DOSs peaks are different; however, all three pairs of densities of states are qualitatively similar before and after structural optimization.

III. RESULTS AND DISCUSSION

III.I. Calculated Properties of Pristine Single-Walled Nanotubes. Several special conditions need to be fulfilled for a material to be photocatalytically active for water splitting. First of all, the band gap ε_{gap} of the catalyst must be in the visible-light range between 1.5 and 2.7 eV; for the solar intensity distribution, the maximum efficiency can be achieved for a band gap between 2.0 and 2.2 eV. The energy conservation condition requires that both the oxidation and reduction potentials of the H_2O molecule in solution defined thermodynamically (ε_{O_2/H_2O} = −5.67 eV and ε_{H_2/H_2O} = −4.44 eV)[4,5] must be positioned inside the band gap of the photocatalytic electrode. Thus, the following inequalities must hold

$$\varepsilon_{VB} < \varepsilon_{O_2/H_2O} < \varepsilon_{H_2/H_2O} < \varepsilon_{CB} \quad (3)$$

where ε_{VB} and ε_{CB} are the energies of the top of the valence band and the bottom of the conduction band, respectively. To justify the alignment of the calculated band gap edges of transition-metal oxide nanostructures relatively to thermodynamically defined redox potential levels, we calculated earlier the one-electron energies for the corresponding stoichiometric multilayers.[48] Unlike 3D bulk, DFT-LCAO calculations on 2D and 1D periodic systems give qualitatively correct distributions of the discrete energies relative to the zero vacuum level.[5]

Table 1 and Figure 4 present results of the LCAO calculations of the band edge parameters of approximately 40

Table 1. Properties of WS_2 SWNTs as Calculated Using the DFT-LCAO Method (HSE06 Exchange−Correlation Functional)[a]

NT chirality	N_{at}	d_{NT}, nm	E_{strain}, eV	$\Delta\varepsilon_{gap}$, eV	ε_{CB}, eV	ε_{VB}, eV
Armchair (n, n) NT Morphology						
(8, 8)	48	1.48	0.94	1.28	−0.27	−0.31
(10, 10)	60	1.82	0.62	1.63	−0.09	−0.49
(12, 12)	72	2.15	0.44	1.86	0.04	−0.59
(16, 16)	96	2.84	0.26	2.13	0.20	−0.69
(20, 20)	120	3.52	0.17	2.27	0.30	−0.75
(22, 22)	132	3.87	0.14	2.34	0.33	−0.77
(24, 24)	144	4.21	0.11	2.37	0.36	−0.78
(26, 26)	156	4.56	0.10	2.40	0.38	−0.79
(28, 28)	168	4.91	0.08	2.43	0.40	−0.80
(30, 30)	180	5.25	0.07	2.45	0.41	−0.81
(40, 40)	240	6.99	0.04	2.50	0.45	−0.82
(50, 50)	300	8.73	0.03	2.51	0.47	−0.80
(60, 60)	360	10.47	0.02	2.51	0.49	−0.80
(70, 70)	420	12.21	0.01	2.52	0.50	−0.79
Zigzag (n, 0) NT Morphology						
(10, 0)	60	1.15	1.62	0.87	−0.41	−0.05
(12, 0)	72	1.34	1.19	1.14	−0.33	−0.23
(16, 0)	96	1.71	0.71	1.55	−0.14	−0.46
(18, 0)	108	1.91	0.57	1.74	−0.02	−0.53
(20, 0)	120	2.10	0.47	1.84	0.03	−0.58
(21, 0)	126	2.20	0.43	1.91	0.08	−0.60
(22, 0)	132	2.29	0.39	1.94	0.09	−0.62
(24, 0)	144	2.49	0.33	2.04	0.15	−0.65
(26, 0)	156	2.68	0.28	2.09	0.18	−0.68
(28, 0)	168	2.88	0.25	2.16	0.22	−0.70
(30, 0)	180	3.08	0.22	2.20	0.25	−0.72
(40, 0)	240	4.07	0.12	2.36	0.35	−0.78
(50, 0)	300	5.07	0.08	2.44	0.40	−0.80
(60, 0)	360	6.07	0.05	2.48	0.43	−0.82
(70, 0)	420	7.07	0.04	2.50	0.46	−0.82
(80, 0)	480	8.07	0.03	2.51	0.47	−0.81
Chiral ($2n$, n) NT Morphology						
(12, 6)	252	1.68	0.73	1.53	−0.15	−0.44
(16, 8)	336	2.20	0.43	1.89	0.06	−0.60
(20, 10)	420	2.72	0.28	2.11	0.20	−0.68
(24, 12)	504	3.24	0.20	2.23	0.27	−0.73
(28, 14)	588	3.77	0.15	2.32	0.32	−0.76
(30, 15)	630	4.03	0.12	2.36	0.35	−0.78
(32, 16)	672	4.29	0.11	2.39	0.37	−0.79
monolayer			0.00	2.53	0.54	−0.76

[a]The number of atoms per 1D periodically repeated NT unit cell, N_{at}; the optimized nanotube diameter, d_{NT}; the strain energy of the corresponding 2D periodic monolayer, E_{strain}, defined as the difference per formula unit between the corresponding energies of single ML and SWNT; the band gap, $\Delta\varepsilon_{gap}$, the positions of the bottom of the conduction band relative to the H_2/H_2O reduction potential or standard hydrogen electrode (SHE); ε_{CB} (positive sign means that the band gap edge is lying above the SHE level); and the positions of the top of the valence band with respect to the O_2/H_2O oxidation potential; ε_{VB} (negative sign means that the band edge is below the ε_{O_2/H_2O} level). Data are given for achiral armchair (n, n) and zigzag (n, 0) as well as for chiral ($2n$, n) WS_2 SWNTs.

DOI: 10.1021/acsomega.8b03121
ACS Omega 2019, 4, 1434−1442

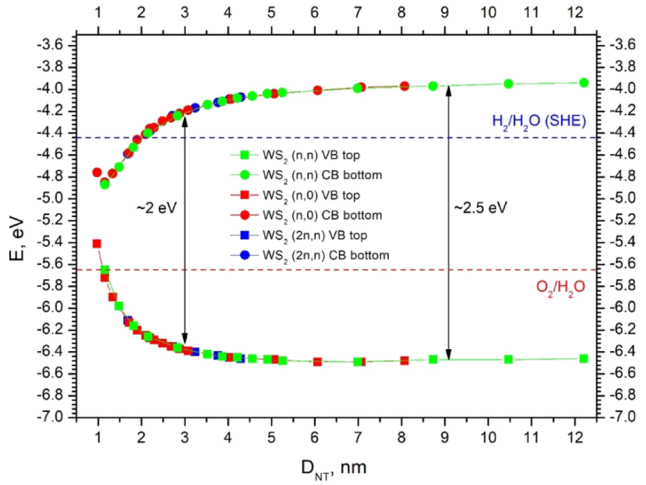

Figure 4. Dependence of valence band and conduction band edges on WS_2 NT diameter for three different configurations: achiral (n, n) and $(n, 0)$, as well as chiral $(2n, n)$. Energy is referenced to a vacuum level.

different WS_2 nanotubes, including the position of the top of the valence band and the bottom of the conduction band relative to the reduction and oxidation potentials of water, ε_{H_2/H_2O} and ε_{O_2/H_2O}, respectively. One can see that the top of the valence band of NTs with $d_{NT} \geq 1.9$ nm is positioned below the ε_{O_2/H_2O} level; thus, the first part of eq 3 is satisfied for all SWNTs.

For small SWNTs ($d_{NT} < 1.9$ nm), the bottom of the conduction band is located below the ε_{H_2/H_2O} level, which prevents the catalytic decomposition of H_2O. However, an increase in the diameter leads to a rapid shift of the ε_{CB} level upward, and thus eq 3 is valid for all nanotubes of diameter $d_{NT} \geq 1.9$ nm, irrespective of chirality. The width of the optical band gap $\Delta\varepsilon_{gap}$ ranges from 0.87 to 2.52 eV, and it increases rapidly with increasing diameter and satisfies eq 3 for all diameters $d_{NT} \geq 1.9$ nm. Optimum values of the band gap, $\Delta\varepsilon_{gap}$ (in the range of 2.0−2.2 eV) correspond to nanotubes with diameters between 2 and 3 nm.

Figure 4 displays the band gap edges graphically for the WS_2 SWNTs with the three considered configurations (see Figure 1). A straightforward observation is that the band gap edges depend only on NT diameter and are identical for NTs with the same diameter, independent of morphology. It is obvious that for very narrow NTs with $d_{NT} < 1.0$ nm, the gap width is smaller than the critical value of 1.23 eV, with both the VB top and CB bottom located between the redox levels.

The band gap widens and the edges move in opposite directions, approaching a limiting value with an approximately exponential dependence on NT diameter. At $d_{NT} \sim 3$ nm, the value of $\Delta\varepsilon_{gap}$ reaches 2.0 eV, which, as was mentioned earlier, corresponds to an approximately optimal average value for a water-splitting photocatalyst under sunlight irradiation. It should also be noted that the CB bottom is closer to the critical H_2/H_2O reduction potential or standard hydrogen electrode (SHE) level than the VB top is to the oxidation potential ε_{O_2/H_2O}. Upon further increase beyond 3 nm, the band gap growth is less steep, converging to ~2.5 eV, which is regarded as the upper bound of an optimal band gap. The CB bottom is still closer to its neighboring reduction level than the VB top is to the value of ε_{O_2/H_2O}.

III.II. Calculated Properties of Multiwalled Pristine Nanotubes. For MWNTs, only their achiral configurations have been modeled (Figures 2 and 3), due to the high computation costs for the chiral $(2n, n)$ NTs, whose unit cells contain a large numbers of atoms (Figure 1c). Several configurations were considered for DWNTs. The largest diameter of the outer NT was 7.07 nm for the $(n, 0)$ configuration and 10.4 nm for (n, n) NTs (Figure 5). The

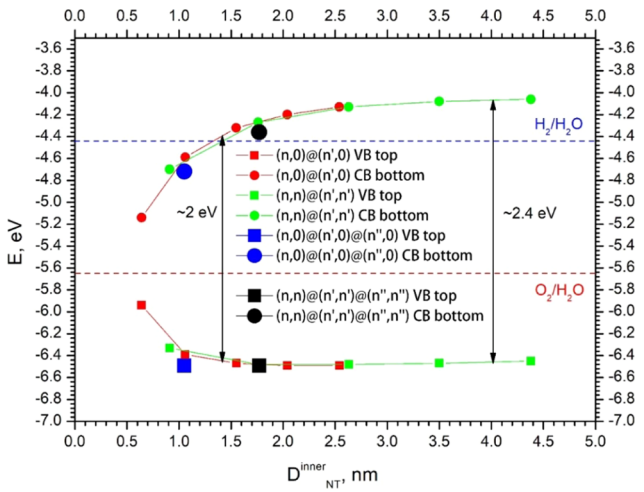

Figure 5. Dependence of valence band and conduction band edges on the inner diameter of double- and triple-walled WS_2 nanotubes. Energy is referenced to a vacuum level.

choice of wall pairs was driven by the desire to keep the optimized interwall distances as close to the experimental value of 6.3−6.5 Å as possible,[49] while keeping the number of atoms in the elementary cell small. This objective is not perfectly fulfilled, since the rototranslational symmetry exploited in the CRYSTAL computational code[32] requires that the two (or three) NT shells are commensurate. We thus chose MWNTs with differences between the chirality indices to be multiples of 10, e.g., (40, 40)@(30, 30), to reduce computational costs to a feasible level.

Five different DW configurations have been modeled (Table 2). A consistent observation is that the band gap of DWNT is always slightly narrower than the gaps of each of the individual constituent SWNTs. The difference values in the range of tens of meV are characteristic for van der Waals interactions between the two layers. This effect is even more prominent for the TWNTs, when we compare the positions of the CB bottom for the TWNT and the (20, 0) model. Unfortunately, for TWNTs, the shift of the CB edge becomes detrimental for photocatalysis. For DWNTs, the effect is ambivalent: for the smaller NTs, the CB edge shift is excessive, while for the larger NTs, it becomes favorable. All results calculated for DW and TWNTs are systematized in Figure 5.

In the case of TWNTs, only one specific variation has been considered for each achiral configuration (Figure 3), to construct a triple-wall nanotube from the previously modeled SWNTs with the condition of keeping the interwall distance realistic and using only multiples of 10 for the chirality indices so as to facilitate symmetry exploitation at a reasonable computational cost. The calculated properties of the two TWNTs are combined in Table 2 to those of DWNTs. The aforementioned conclusions for the $(n, 0)$ NTs are also applicable in the case of the (n, n) NTs: the presence of the

DOI: 10.1021/acsomega.8b03121
ACS Omega 2019, 4, 1434−1442

Table 2. Properties of MW WS_2 NTs as Calculated Using the DFT-LCAO Method (Applying the HSE06 Exchange–Correlation Functional)[a]

NT's chiralities	N_{at}	d_{NT}, nm outer	d_{NT}, nm middle	d_{NT}, nm inner	E_{form}, meV	$\Delta\varepsilon_{gap}$, eV	ε_{CB}, eV	ε_{VB}, eV
Armchair MW NT Morphology								
(20, 20)@(10, 10)	180	1.76		0.91	−4.3	1.63	−0.26	−0.66
(30, 30)@(20, 20)	300	2.62		1.76	−0.46	2.21	0.17	−0.81
(40, 40)@(30, 30)	420	3.49		2.63	−0.60	2.35	0.31	−0.81
(50, 50)@(40, 40)	540	4.36		3.50	−0.67	2.39	0.36	−0.80
(60, 60)@(50, 50)	660	5.21		4.38	−0.63	2.39	0.38	−0.78
(40, 40)@(30, 30)@(20, 20)	540	3.49	2.63	1.77	−0.66	2.13	0.08	−0.82
Zigzag MW NT Morphology								
(30, 0)@(10, 0)	240	1.54		0.64	4.37	0.80	−0.70	−0.27
(40, 0)@(20, 0)	360	2.04		1.06	0.18	1.80	−0.15	−0.72
(50, 0)@(30, 0)	480	2.53		1.55	0.01	2.15	0.12	−0.80
(60, 0)@(40, 0)	600	3.04		2.04	−0.02	2.29	0.24	−0.82
(70, 0)@(50, 0)	720	3.54		2.54	0.01	2.36	0.31	−0.82
(60, 0)@(40, 0)@(20, 0)	720	3.04	2.04	1.05	1.15	1.77	−0.28	−0.82
monolayer						2.53	0.54	−0.76

[a]Number of atoms per 1D periodically repeated NT unit cell, N_{at}; optimized diameters of NT shells, d_{NT} (outer, middle, and inner); interwall interaction energy per formula unit, E_{int} defined by eqs 2a and 2b in Section II.II (their negative or positive sign denotes interwall attraction or repulsion, respectively); band gap, $\Delta\varepsilon_{gap}$; positions of the bottom of the conduction band relative to the standard hydrogen electrode SHE potential, ε_{CB} (negative sign means that the band edge is lying below the ε_{H_2/H_2O} level), and positions of the top of the valence band with respect to the O_2/H_2O oxidation potential, ε_{VB} (negative sign means that the band edge is lying below the ε_{O_2/H_2O} level).

van der Waals-induced band gap reduction effect for MWNTs is visible; it is, however, less prominent for the (n, n) TWNTs compared to their $(n, 0)$ analogues. In any case, for the larger DWNTs, the suitability for photocatalytical water splitting is higher than for their SW constituents.

Table 2 also shows that the interwall interactions E_{int} estimated using eqs 2a and 2b are predominantly attractive in WS_2 MWNTs with armchair configuration, while they are mainly repulsive for zigzag-type NTs. In any case, the absolute values of E_{int} increase with decreasing interwall distances. However, these interactions are found to be very weak (about 50−500 times smaller) in comparison to those in DW V_2O_5 nanotubes.[50] These differences may be due to strong Coulomb interactions, which dominate the interactions between the inner and outer walls of transition-metal-oxide DWNTs, whereas the interaction in metal sulfide DWNTs is the result of van der Waals and weak electrostatic interactions.

III.III. Comparison of DOSs for WS_2 SWNTs Calculated Using DFT-LCAO and DFT-LACW Methods. Figure 6 compares the total and projected densities of states (DOS) calculated using the DFT-LCAO (left) and DFT-LACW (right) methods for [0001]-oriented WS_2 NTs with chirality indexes (12, 12), (16, 8), and (21, 0) (Figure 1), which all have a diameter of ∼2.2 nm (Table 1). The LCAO and LACW calculations on WS_2 SWNTs allow us to perform an orbital analysis of the projected DOS to clarify their natural chemical composition. Independent of chirality, in all studied pristine WS_2 NTs, the upper part of the VB is predominantly formed by the S (3p) orbitals with significant contributions from W (5d) orbitals, except for the outermost range of the VB, where LCAO calculations provide noticeably larger contributions from W (5d) orbitals. LACW calculations also produce qualitatively similar results for the armchair (12, 12) WS_2 SWNT. This is in line with results of our recent calculations performed using the LCAO approach for both single- and multilayered WS_2(0001) nanofilms,[40] where each valence band can be divided into two parts: the wide bottom one, with dominant contributions from S (3p) orbitals, and the outermost states have a larger contribution from W (5d) orbitals. In contrast, results obtained when using both LCAO and LACW calculations clearly show that the bottom-most parts of the conduction band are formed mainly by W (5d) states with a partial contribution from S (3p) states.

For either calculation method (LCAO and LACW), the top of the valence band is positioned well below the oxidation potential O_2/H_2O, irrespective of the NT chirality and independent of the diameter of the nanotubes (Figure 4). Interestingly, the bottom of the conduction band for the (12, 12), (21, 0), and (16, 8) WS_2 NTs with diameter of 2.2 nm is positioned almost exactly at the reduction potential, ε_{H_2/H_2O}. Hence, hydrogen evolution is possible for water splitting with the WS_2 NT photocatalyst, when the nanotube diameter is larger than ∼1.9 nm, as mentioned above. On the whole, both methods of computation are qualitatively compatible for the description of the DOSs. Figures 4 and 6 thus confirm the potential suitability of pristine single-walled WS_2 nanotubes for photocatalytic applications.

IV. SUMMARY AND CONCLUSIONS

We have simulated the electronic structure of pristine single-walled WS_2 NTs of three different types of chirality (Figure 1) as a function of nanotube diameter. The band edges depend in all of the cases only on the diameter d_{NT} (and not on the chirality indices of the nanotubes). For d_{NT} > 1.9 nm, the energy diagrams for WS_2 SWNTs (Figure 4) support the potential ability of the NTs to serve as photocatalysts for water-splitting reactions. In this diameter range, the necessary condition for the ordering of energies, $\varepsilon_{VB} < \varepsilon_{O_2/H_2O} < \varepsilon_{H_2/H_2O} < \varepsilon_{CB}$,[5] is fulfilled. Thus, by choosing the NT diameter appropriately, the band gap can be tuned with high-energy resolution, which makes WS_2 SWNTs suitable for photocatalytic applications in the visible spectrum.

In addition, we have computed the electronic structure of several selected double- and triple-walled WS_2 nanotubes with armchair- (n, n) and zigzag-type $(n, 0)$ configurations (Figures

DOI: 10.1021/acsomega.8b03121
ACS Omega 2019, 4, 1434−1442

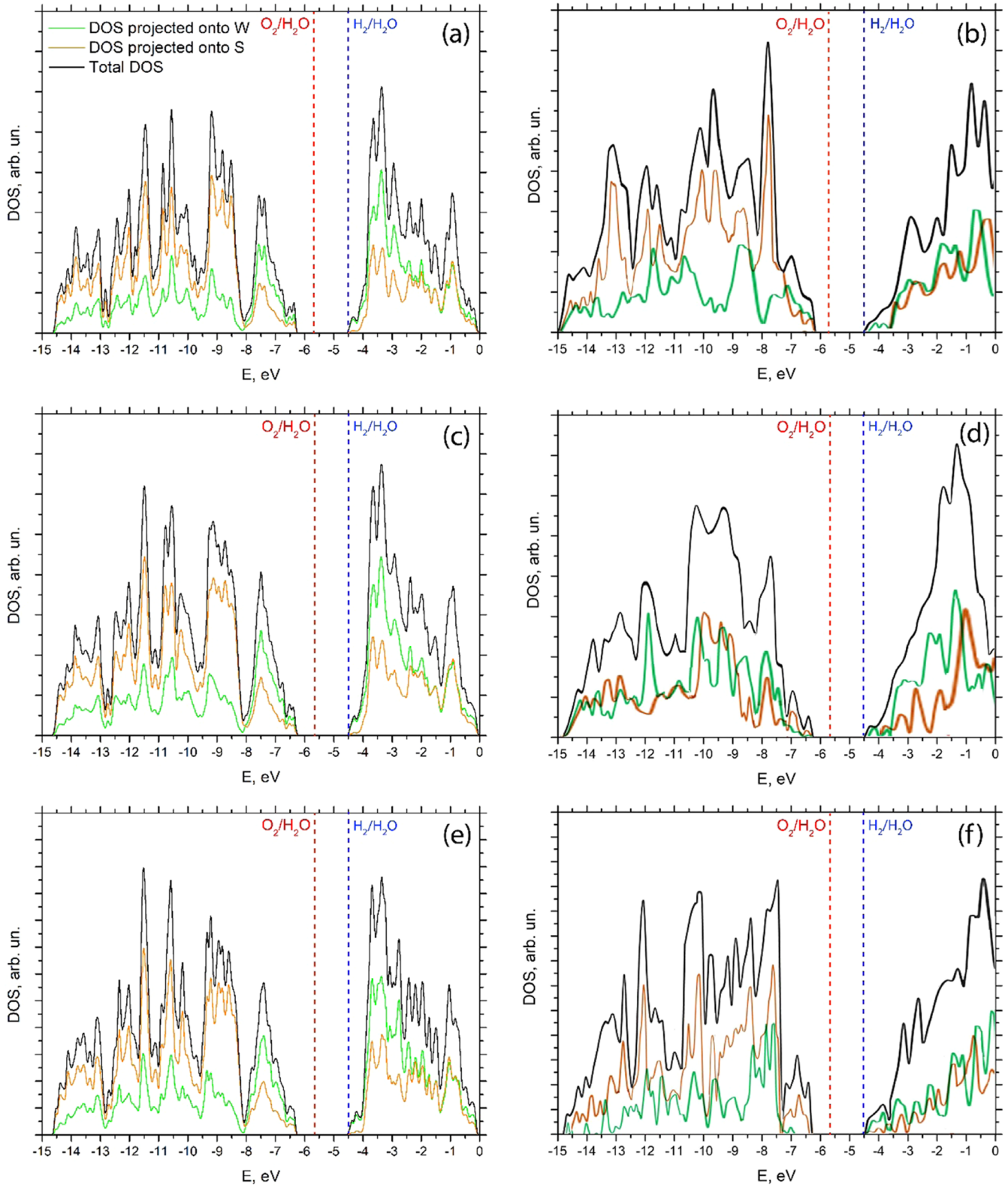

Figure 6. Total and projected electronic densities of states (DOSs) calculated for the (12, 12), (16, 8), and (21, 0) SWNTs using the DFT-LCAO (a, c, e) and DFT-LACW (b, d, e) methods, respectively. The effect of crossing between the vertical SHE line and the bottom of the conduction band in all of the plots (a–f) is caused by Gaussian semiextension of each DOS peak. In reality, a small gap between them exists as follows from Figure 4.

2 and 3), which have not been simulated so far. It has been found that the value of $\Delta\varepsilon_{gap}$ is smaller than the corresponding values for each of its constituents (cf. Figures 4 and 5) caused by the influence of interwall interactions. This further increases the variability of possible energy ranges suitable for photocatalysis.

Hence, in summary, for pristine WS_2 nanotubes with diameters in the range of 2−12 nm, the energies of the optical

DOI: 10.1021/acsomega.8b03121
ACS Omega 2019, 4, 1434−1442

gaps, the positions of the top of the valence band and the bottom of the conduction band relative to the oxidation and reduction potentials of the H_2O medium are suitable for the photochemical splitting of water and hydrogen production under solar irradiation. In the next stage of our study, we plan to perform molecular dynamics simulations of the interactions of water films with the WS_2 nanosubstrate, analogous to our recent work for the H_2O/TiO_2 system.[51]

AUTHOR INFORMATION

Corresponding Author

*E-mail: piskunov@lu.lv.

ORCID

Sergei Piskunov: 0000-0002-8768-0736
Pavel N. D'yachkov: 0000-0003-2840-5555
Stephane Kenmoe: 0000-0003-3622-2716

Notes

The authors declare no competing financial interest.

ACKNOWLEDGMENTS

This study was supported by the EC ERA.Net RUS Plus project No. 237 WATERSPLIT as well as Russian Basic Research Foundation No. 16-53-76019. S.K. and E.S. furthermore gratefully acknowledge computing time granted by the Center for Computational Sciences and Simulation (CCSS) of the Universität Duisburg-Essen and the supercomputer magnitUDE (DFG grants INST 20876/209-1 FUGG, INST 20876/243-1 FUGG) provided by the Zentrum für Informations- und Mediendienste (ZIM). E.S. is also grateful for support by the Cluster of Excellence RESOLV (EXC1069) funded by the Deutsche Forschungsgemeinschaft.

REFERENCES

(1) Fujishima, A.; Honda, K. Electrochemical Photolysis of Water at a Semiconductor Electrode. *Nature* **1972**, 37−38.

(2) Thimsen, E.; Biswas, S.; Lo, C. S.; Biswas, P. Predicting the band structure of mixed transition metal oxides: Theory and experiment. *J. Phys. Chem. C* **2009**, *113*, 2014−2021.

(3) Kumar, S. G.; Devi, L. G. Review on modified TiO_2 photocatalysis under UV/visible light: selected results and related mechanisms on interfacial charge carrier transfer dynamics. *J. Phys. Chem. A* **2011**, *115*, 13211−13241.

(4) Chen, X.; Shen, S.; Guo, L.; Mao, S. S. Semiconductor-based Photocatalytic Hydrogen Generation. *Chem. Rev.* **2010**, *110*, 6503−6570.

(5) Zhukovskii, YuF.; Piskunov, S.; Lisovski, O.; Bocharov, D.; Evarestov, R. A. Doped 1D nanostructures of transition-metal oxides: first-principles evaluation of photocatalytic suitability (Review). *Isr. J. Chem.* **2017**, *57*, 461−476.

(6) Braga, D.; Gutiérrez Lezama, I.; Berger, H.; Morpurgo, A. F. Quantitative determination of the band gap of WS_2 with ambipolar ionic liquid-gated transistors. *Nano Lett.* **2012**, *12*, 5218−5223.

(7) Schutte, W.; De Boer, J. L.; Jellinek, F. Crystal structures of tungsten disulfide and diselenide. *J. Solid State Chem.* **1987**, *70*, 207−209.

(8) Decker, F.; Scrosati, B.; Razzini, G. Photoelectrochemical solar cells based on molybdenum and tungsten dichalcogenides. In *Photoelectrochemistry and Photovoltaics of Layered Semiconductors*; Aruchamy, A., Ed.; Kluwer Acad. Publishers: Dordrecht, 1992; pp 121−153.

(9) Haque, F.; Daeneke, T.; Kalantar-zadeh, K.; Ou, J. Z. Two-dimensional transition metal oxide and chalcogenide-based photocatalysts. *Nano-Micro Lett.* **2018**, *10*, 1−27.

(10) Zhao, W.; Ghorannevis, Z.; Chu, L.; Toh, M.; Kloc, C.; Tan, P. H.; Eda, G. Evolution of electronic structure in atomically thin sheets of WS_2 and WSe_2. *ACS Nano* **2013**, *7*, 791−797.

(11) Zhang, Y.; Zhang, Y.; Ji, Q.; Ju, J.; Yuan, H.; Shi, J.; Gao, T.; Ma, D.; Liu, M.; Chen, Y.; Song, X.; Hwang, H. Y.; Cui, Y.; Liu, Z. Controlled growth of high-quality monolayer WS_2 layers on sapphire and imaging its grain boundary. *ACS Nano* **2013**, *7*, 8963−8971.

(12) Ramakrishna Matte, H. S. S.; Gomathi, A.; Manna, A. K.; Late, D. J.; Datta, R.; Pati, S. K.; Rao, C. N. R. MoS_2 and WS_2 analogues of graphene. *Angew. Chem., Int. Ed.* **2010**, *122*, 4153−4156.

(13) Mahler, B.; Hoepfner, V.; Liao, K.; Ozin, G. A. Colloidal synthesis of 1*T*-WS_2 and 2*H*-WS_2 nanosheets: Applications for photocatalytic hydrogen evolution. *J. Am. Chem. Soc.* **2014**, *136*, 14121−14127.

(14) Sang, Y.; Zhao, Z.; Zhao, M.; Hao, P.; Leng, Y.; Liu, H. From UV to near-infrared, WS_2 nanosheet: A novel photocatalyst for full solar light spectrum photodegradation. *Adv. Mater.* **2015**, *27*, 363−369.

(15) Vattikuti, S. V. P.; Byon, C.; Chitturi, V. Selective hydrothermally synthesis of hexagonal WS_2 platelets and their photocatalytic performance under visible light irradiation. *Superlattices Microstruct.* **2016**, *94*, 39−50.

(16) Salehi, S.; Saffarzadeh, A. Atomic defect states in monolayers of MoS_2 and WS_2. *Surf. Sci.* **2016**, *651*, 215−221.

(17) Shang, X.; Yan, K.-L.; Liu, Z.-Z.; Lu, S.-S; Dong, B.; Chi, J.-Q.; Li, X.; Liu, Y.-R.; Chai, Y.-M.; Liu, C.-G. Oxidized carbon fiber supported vertical WS_2 nanosheets arrays as efficient 3D nanostructure electrocatalysts for hydrogen evolution reaction. *Appl. Surf. Sci.* **2017**, *402*, 120−128.

(18) Tenne, R.; Margulis, L.; Genut, M.; Hodes, G. Polyhedral and cylindrical structures of tungsten disulphide. *Nature* **1992**, *360*, 444−446.

(19) Rothschild, A.; Cohen, S. R.; Tenne, R. WS_2 nanotubes as tips in scanning probe microscopy. *Appl. Phys. Lett.* **1999**, *75*, 4025−4027.

(20) Zhu, Y. Q.; Hsu, W. K.; Firth, S.; Terrones, M.; Clark, R. J. H.; Kroto, H. W.; Walton, D. R. M. Nb-doped WS_2 nanotubes. *Chem. Phys. Lett.* **2001**, *342*, 15−21.

(21) Zibouche, N.; Kuc, A.; Heine, T. From layers to nanotubes: Transition metal disulfides TMS_2. *Eur. Phys. J. B* **2012**, *85*, 1−7.

(22) Yadgarov, L.; Rosentsveig, R.; Leitus, G.; Albu-Yaron, A.; Moshkovich, A.; Perfilyev, V.; Vasic, R.; Frenkel, A. I.; Enyashin, A. N.; Seifert, G.; Rapoport, L.; Tenne, R. Controlled doping of MS_2 (M = W, Mo) nanotubes and fullerene-like nanoparticles. *Angew. Chem., Int. Ed.* **2012**, *51*, 1148−1151.

(23) Tsverin, Y.; Livneh, T.; Rosentsveig, R.; Zak, A.; Pinkas, I.; Tenne, R. Photocatalysis with hybrid Co-coated WS_2 nanotubes. *Nanomater. Energy* **2013**, *2*, 25−34.

(24) Levi, R.; Bitton, O.; Leitus, G.; Tenne, R.; Joselevich, E. Field-effect transistors based on WS_2 nanotubes with high current-carrying capacity. *Nano Lett.* **2013**, *13*, 3736−3741.

(25) O'Neal, K. R.; Cherian, J. G.; Zak, A.; Tenne, R.; Liu, Z.; Musfeldt, J. L. High pressure vibrational properties of WS_2 nanotubes. *Nano Lett.* **2016**, *16*, 993−999.

(26) Damnjanović, M.; Vuković, T.; Milošević, I. Symmetry-based study of MoS_2 and WS_2 nanotubes (Review). *Isr. J. Chem.* **2017**, *57*, 450−460.

(27) Evarestov, R. A.; Bandura, A. V.; Porsev, V. V.; Kovalenko, A. V. Phonon spectra, electronic, and thermodynamic properties of WS_2 nanotubes. *J. Comput. Chem.* **2017**, *38*, 2581−2593.

(28) Xiao, S. L.; Yu, W. Z.; Gao, S. P. Edge preference and band gap characters of MoS_2 and WS_2 nanoribbons. *Surf. Sci.* **2016**, *653*, 107−112.

(29) James, D.; Zubkov, T. Photocatalytic properties of free and oxide-supported MoS_2 and WS_2 nanoparticles synthesized without surfactants. *J. Photochem. Photobiol., A* **2013**, *262*, 45−51.

(30) Ho, W.; Yu, J. C.; Lin, J.; Yu, J.; Li, P. Preparation and photocatalytic behavior of MoS_2 and WS_2 nanocluster sensitized TiO_2. *Langmuir* **2004**, *20*, 5865−5869.

DOI: 10.1021/acsomega.8b03121
ACS Omega 2019, 4, 1434−1442

(31) Saito, R.; Dresselhaus, M. S.; Dresselhaus, G. *Physical Properties of Carbon Nanotubes*; Imperial College Press, World Scientific Publishing Co. Pte. Ltd.: Singapore, 1998.
(32) Dovesi, R.; Saunders, V. R.; Roetti, C.; Orlando, R.; Zicovich-Wilson, C. M.; Pascale, F.; Civalleri, B.; Doll, K.; Harrison, N. M.; Bush, I. J.; D'Arco, P.; Llunell, M.; Causá, M.; Noël, Y. *CRYSTAL14 User's Manual*; University of Torino, 2014.
(33) Polyakov, B.; Kuzmin, A.; Smits, K.; Zideluns, J.; Butanovs, E.; Butikova, J.; Vlassov, S.; Piskunov, S.; Zhukovskii, YuF. Unexpected epitaxial growth of a few WS_2 layers on $\{1\bar{1}00\}$ facets of ZnO nanowires. *J. Phys. Chem. C* **2016**, *120*, 21451−21459.
(34) Perdew, J. P.; Burke, K.; Ernzerhof, M. Generalized gradient approximation made simple. *Phys. Rev. Lett.* **1996**, *77*, 3865−3868.
(35) Krukau, A. V.; Vydrov, O. A.; Izmaylov, A. F.; Scuseria, G. E. Influence of the exchange screening parameter on the performance of screened hybrid functionals. *J. Chem. Phys.* **2006**, *125*, No. 224106.
(36) Peintinger, M. F.; Oliveira, D. V.; Bredow, T. Consistent gaussian basis sets of triple-zeta valence with polarization quality for solid-state calculations. *J. Comput. Chem.* **2013**, *34*, 451−459.
(37) Bandura, A. V.; Evarestov, R. A. Structure and stability of SnS_2-based single- and multi-wall nanotubes. *Surf. Sci.* **2015**, *641*, 6−15.
(38) Monkhorst, H. J.; Pack, J. D. Special points for Brillouinzone integrations. *Phys. Rev. B* **1976**, *13*, 5188−5192.
(39) Grimme, S. Semi-empirical GGA-type density functional constructed with a long-range dispersion correction. *J. Comput. Chem.* **2006**, *27*, 1787−1799.
(40) Bocharov, D.; Piskunov, S.; Zhukovskii, Y. F.; Evarestov, R. A. *Ab initio* calculations on the electronic structure and photocatalytic properties of two-dimensional WS_2 (0001) nanolayers of varying thickness. *Phys. Status Solidi RRL* **2018**, *12*, No. 1800253.
(41) Ghorbani-Asl, M.; Zibouche, N.; Wahiduzzaman, M.; Oliveira, A. F.; Kuc, A.; Heine, T. Electromechanics in MoS_2 and WS_2: nanotubes vs monolayers. *Sci. Rep.* **2013**, *3*, No. 02961.
(42) D'yachkov, P. N. Linear augmented cylindrical wave method for nanotubes electronic structure. *Int. J. Quantum Chem.* **2016**, *116*, 174−188.
(43) D'yachkov, P. N.; Makaev, D. V. Account of helical and rotational symmetries in the linear augmented cylindrical wave method for calculating the electronic structure of nanotubes: towards the ab initio determination of the band structure of a (100, 99) tubule. *Phys. Rev. B* **2007**, *76*, No. 195411.
(44) D'yachkov, P. N.; Kutlubaev, D. Z.; Makaev, D. V. Linear augmented cylindrical wave green's function method for electronic structure of nanotubes with substitutional impurities. *Phys. Rev. B* **2010**, *82*, No. 035426.
(45) Zhukovskii, Y. F.; Piskunov, S.; Kazerovskis, J.; Makaev, D. V.; D'yachkov, P. N. Comparative Theoretical Analysis of BN Nanotubes Doped with Al, P, Ga, As, In, and Sb. *J. Phys. Chem. C* **2013**, *117*, 14235−14240.
(46) D'yachkov, P. N.; Zaluev, V. A.; Piskunov, S. N.; Zhukovskii, Y. F. Comparative analysis of the electronic structures of mono- and bi-atomic chains of IV, III-V and II-VI group elements calculated using the DFT LCAO and LACW methods. *RSC Adv.* **2015**, *5*, 91751−91759.
(47) D'yachkov, P. N. Augmented waves for nanomaterials. In *Encyclopedia of Nanoscience and Nanotechnology*, 1st ed.; Nalwa, N. S., Ed.; Amer. Sci. Publishers, 2004; pp 191−212.
(48) Piskunov, S.; Lisovski, O.; Begens, J.; Bocharov, D.; Zhukovskii, YuF.; Wessel, M.; Spohr, E. C-, N-, S-, and Fe-doped TiO_2 and $SrTiO_3$ nanotubes for visible-light driven photocatalytic water splitting: Prediction from first principles. *J. Phys. Chem. C* **2015**, *119*, 18686−18696.
(49) Brüser, V.; Popovitz-Biro, R.; Albu-Yaron, A.; Lorenz, T.; Seifert, G.; Tenne, R.; Zak, A. Single to triple-wall WS_2 nanotubes obtained by high-power plasma ablation of WS_2 multiwall nanotubes. *Inorganics* **2014**, *2*, 177−190.
(50) Porsev, V. V.; Bandura, A. V.; Evarestov, R. A. Theoretical Study of α-V_2O_5-Based Double-Wall Nanotubes. *ChemPhysChem* **2015**, *16*, 3007−3014.
(51) Kenmoe, S.; Lisovski, O.; Piskunov, S.; Bocharov, D.; Zhukovskii, YuF.; Spohr, E. Water adsorption on clean and defective anatase TiO_2 (001) nanotube surfaces: A surface science approach. *J. Phys. Chem. B* **2018**, *122*, 5432−5440.

DOI: 10.1021/acsomega.8b03121
ACS Omega 2019, 4, 1434−1442